Operational range of a ferrofluid pocket bearing

Boots, Jelle; Spronck, Jo; van Ostayen, Ron; Lampaert, Stefan

DOI
10.1088/1361-665X/ab2b60

Publication date
2019

Document Version
Final published version

Published in
Smart Materials and Structures

Smart Materials and Structures

PAPER • **OPEN ACCESS**

Operational range of a ferrofluid pocket bearing

To cite this article: A S T Boots *et al* 2019 *Smart Mater. Struct.* **28** 115030

OPEN ACCESS
IOP Publishing
Smart Materials and Structures
Smart Mater. Struct. **28** (2019) 115030 (13pp)
https://doi.org/10.1088/1361-665X/ab2b60

Operational range of a ferrofluid pocket bearing

A S T Boots, J W Spronck, R A J van Ostayen and S G E Lampaert

Department of Precision and Microsystems Engineering, Delft University of Technology, Mekelweg 2, 2628CD, Delft, The Netherlands

E-mail: S.G.E.Lampaert@tudelft.nl

Received 17 December 2018, revised 8 April 2019
Accepted for publication 20 June 2019
Published 16 October 2019

Abstract

Ferrofluid pocket bearings are interesting for fast and precise positioning systems thank to the absence of stick-slip, the low viscous friction and their cost-effective nature. However, the characteristics of the bearing change due to over(de)compression since air escapes out of the enclosed pocket. This article presents an experimentally validated model that includes the air mass inside the pocket in the calculation of the equilibrium position of the ferrofluid bearing. Moreover, a simple and efficient way to obtain the operational range of the bearing is presented and a sensitivity analysis was performed. The sensitivity analysis showed that ferrofluid pocket bearings are always self-aligning and that the tilt stiffness increases when the fly height decreases or the tilt angle increases.

Supplementary material for this article is available online

Keywords: precision engineering, numerical modelling, hydrostatic bearing, magnetism, sensitivity analysis, rotational stiffness, sealing capacity

(Some figures may appear in colour only in the online journal)

1. Introduction

A ferrofluid is a colloidal suspension of small magnetic particles inside a carrier fluid. The magnetic particles (3–15 nm), often covered with a layer of dispersant, give the fluid paramagnetic properties [1–3].

Numerous applications have been suggested for ferrofluids over the years [4–7], ranging from sensors [8, 9] and actuators [10–14] to the use of ferrofluid as a lubricant [15] or an energy harvester [16]. Another frequently suggested application is to make staged [17] and non-bursting [18] ferrofluidic seals. This enables rotary shafts to be sealed without the common disadvantage of wear [19, 20], like in vacuum feedthrough [21] or aqueous environments [22]. Ferrofluid bearings and seals can be optimised by maximising the magnetic force generated by permanent magnets using ferromagnetic material [23–25]. The absence of stick-slip also makes ferrofluid bearings useful in high precision systems [26–30].

Ferrofluid bearings can be classified as either pressure bearings or pocket bearings [31]. Ferrofluid pressure bearings only rely on the pressure inside the ferrofluid to carry a load. Pocket bearings on the other hand rely on both the pressurised air pocket, which is encapsulated by the ferrofluid seal, and the pressure inside the seal itself. The pressure is a result of the magnetic body force which depends on the external magnetic field and the boundary condition of the magnetic fluid [32, 33].

Lampaert *et al* [34] presented a mathematical model to calculate the maximum load capacity of ferrofluid pocket bearings. Over(de)compression of a ferrofluid pocket bearing resulted in air escaping in and out of the pocket which subsequently changed the behaviour of the bearing. However, the bearing also showed good repeatability over multiple compression-decompression cycles when the mass inside the pocket is unaltered. In practice, this is the operational range of the bearing.

In this article, the behaviour of the bearing after over(de)compression is modelled to determine its operational range. First, an experimentally validated model is presented to

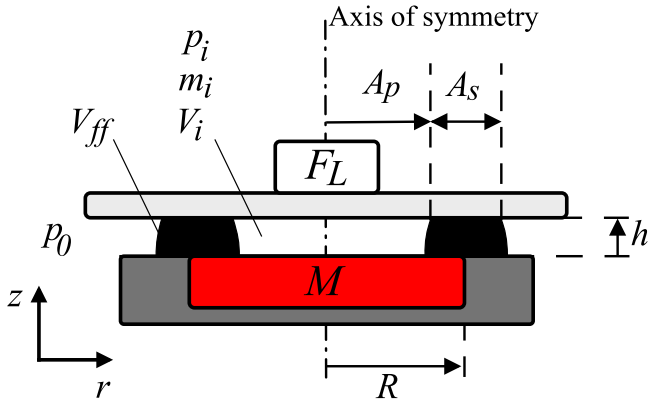

Figure 1. A cross-section of the ferrofluid pocket bearing defines the parameters used in this article. The cylindrical magnet, with magnetisation M, is placed in a non-ferromagnetic base (grey).

calculate the position of the ferrofluid seal depending on the air mass inside the pocket. Next, this position will be used to calculate the load capacity of the ferrofluid bearing according to literature. Moreover, a simple and efficient way to obtain the operational range is presented based on only the strength of a ferrofluid seal and the mass inside the pocket. Finally, a sensitivity study was performed in order to see how different variables affect the load capacity and operational range of the bearing.

2. Methods

First, the calculation of the strength of a ferrofluid seal in the presence of an external magnetic field is described. Subsequently, the load capacity of the bearing is derived and the sensitivity of the load capacity with respect to tilt is analysed. The sensitivity can be used to determine how the bearing performs in practice where disturbances are present. The ideal gas law is introduced to calculate the air mass enclosed by the ferrofluid seal. Next, the finite element method (FEM) model is introduced, which will be used to calculate the positions of the interfaces between ferrofluid and air. The magnitude and positions of the interfaces will subsequently be used to calculate the load capacity and torque of the bearing. The load capacity is calculated according to Lampaert *et al* [34]. Finally, the experimental set-up that was used to validate the predicted load capacity of the bearing is introduced. Figure 1 shows the schematic of the bearing including all the important parameters.

2.1. Mathematical model

2.1.1. Ferrofluid seal. The pressure inside a stationary ferrofluid seal can be derived from the Ferrohydrodynamic Navier–Stokes equations for incompressible Newtonian fluids [2, 35]. In the derivation, it is assumed that the ferrofluid is completely saturated and that the only body force present is the magnetic body force. The result is equation (1) for the pressure distribution inside a ferrofluid [24, 34]. In this equation, the pressure ($p(r)$) inside the ferrofluid at a specific

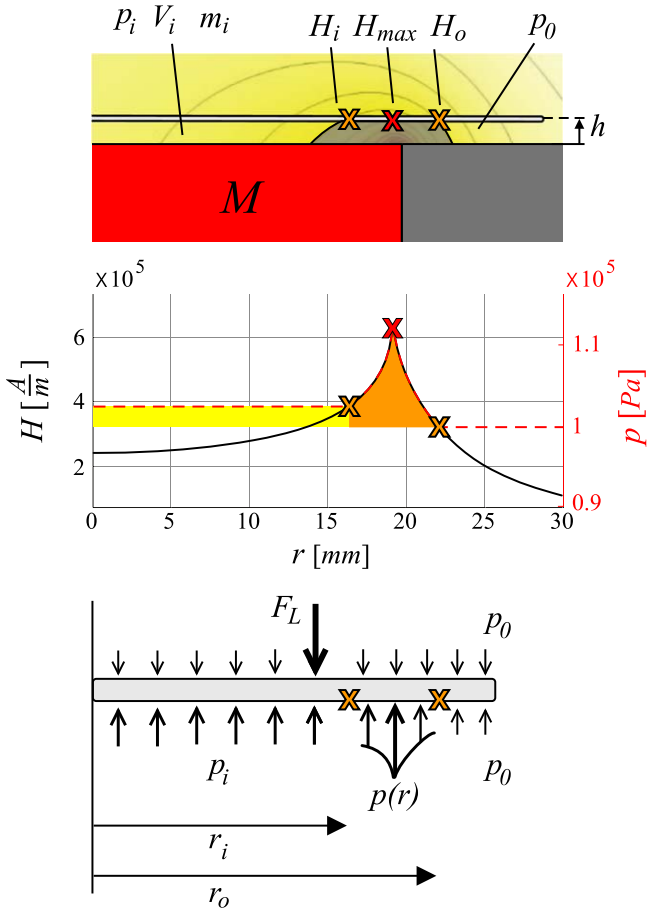

Figure 2. The pressure distribution (middle figure), acting on the plate above the bearing (bottom figure), is a result of the shape and placement of the ferrofluid seal (top figure). The total load capacity is obtained by integrating the pressure distributions given in the bottom figure. The coloured areas in the middle figure represent visually the contributions of the seal and pocket to the total load capacity of the bearing.

radial position (r) and fly height (h), is dependent on the magnetic field intensity ($H(r)$) at that specific location and the magnetic field intensity of the outer fluid-air interface (H_o). Moreover, μ_0 is the permeability of vacuum and M_s the saturation magnetisation of the ferrofluid.

$$p(r) - p_0 = \mu_0 M_s (H(r) - H_o). \tag{1}$$

Equation (1) can be used to calculate the pressure difference over a ferrofluid seal (Δp or $p_i - p_0$) by evaluating the magnetic field intensity at the inner interface (H_i) and at the outer interface (H_o), equation (2). Figure 2 shows the location and shape of the ferrofluid seal for an arbitrary H_i and H_o at h. The figure also shows the resulting pressure distribution.

Next, equation (2) can be used to calculate the maximum pressure difference that a ferrofluid seal can withstand. The maximum pressure difference ($p_{i,max} - p_0$) is determined by the maximum difference in magnetic field intensity that can be achieved across the ferrofluid seal (ΔH or $H_i - H_o$). For the geometries discussed in this article, this maximum is obtained when the inner ferrofluid interface is located at the maximum magnetic field intensity at that specific fly height, thus when $H_i = H_{max}$. This results in equation (4) for the

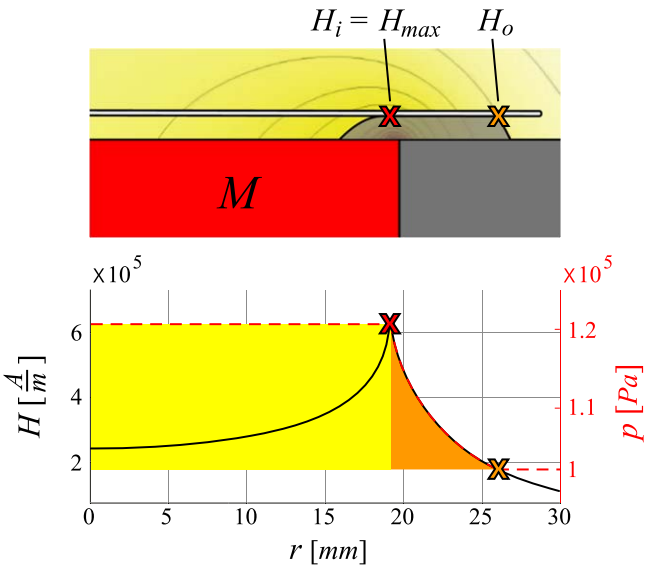

Figure 3. The shape of the ferrofluid seal and the resulting pressure distribution over the seal for a maximum pressurised pocket at a height h. The corresponding load capacity of the seal and the pocket are indicated in orange and yellow.

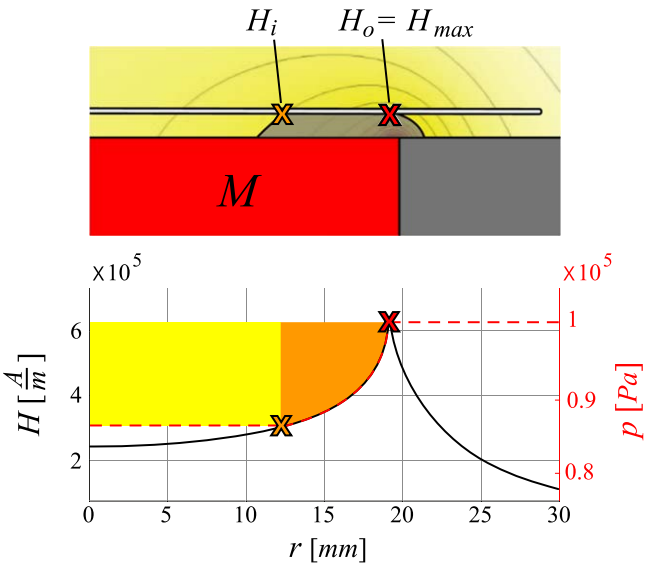

Figure 4. The shape of the ferrofluid seal and the resulting pressure distribution over the seal for a minimum pressurised pocket at a height h. The corresponding load capacity of the seal and the pocket are indicated in orange and yellow.

calculation of the maximum strength of the seal. Note that the value of H_{max} is dependent on the the magnetic field generated by the permanent magnet and the fly height. The value of H_o is dependent on the amount of ferrofluid present in the system (V_{ff}). Figure 3 shows the corresponding location and shape of the seal, the pressure distribution and magnetic field intensity over the seal

$$p_i - p_0 = \mu_0 M_s (H_i - H_o), \tag{2}$$

$$m_i = p_i V_i \frac{M_{air}}{\bar{R}T}. \tag{3}$$

The same reasoning applies to the calculation of the minimum pocket pressure, given in equation (6). In that case, the magnetic field intensity at the outer interface equals the maximum magnetic field intensity at that fly height ($H_o = H_{max}$). This results in a negative pressure drop over the seal, since $H_o > H_i$. Figure 4 shows the shape of the ferrofluid seal for a minimum pressure inside the pocket and once again the pressure distribution and magnetic field for that specific configuration. Note that the pressure inside the pocket is lower than the ambient pressure. The corresponding pressure difference the seal has to withstand is referred to as the minimum strength of the ferrofluid seal

$$p_{i,max} - p_0 = \mu_0 M_s (H_{max} - H_o), \tag{4}$$

$$m_{i,max} = p_{i,max} V_{i,max} \frac{M_{air}}{\bar{R}T}, \tag{5}$$

$$p_{i,min} - p_0 = \mu_0 M_s (H_i - H_{max}), \tag{6}$$

$$m_{i,min} = p_{i,min} V_{i,min} \frac{M_{air}}{\bar{R}T}. \tag{7}$$

2.1.2. Load capacity. Integration of all the different forces that act on the plate (figure 2) results in the total load capacity of the bearing (F_L), equation (8). Combining equations (2) and (8) results in equation (9) for the load capacity expressed in a cylindrical coordinate system. The total load capacity is made up of the contribution of the air pocket and the contribution of the ferrofluid seal. The radial position of the inner interface is denoted by r_i and the outer interface by r_o

$$F_L = \int_0^{2\pi} \int_0^{r_o} (p(r) - p_0) r \, \mathrm{d}r \, \mathrm{d}\theta, \tag{8}$$

$$F_L = \underbrace{\mu_0 M_s (H_i - H_o) \pi r_i^2}_{\text{Air pocket}} + \underbrace{2\pi \mu_0 M_s \int_{r_i}^{r_o} (H(r) - H_o) r \, \mathrm{d}r}_{\text{Ferrofluid seal}}. \tag{9}$$

Figures 2–4 visually show how the load capacity is calculated using equation (8) or (9). The contribution of the pocket to the total load capacity is indicated by the yellow marked area, while that of the seal is marked orange.

The stiffness of the ferrofluid bearing can be calculated by taking the derivative of the load capacity with respect to the vertical position, equation (10)

$$k_z = -\frac{\mathrm{d}F_L}{\mathrm{d}h}. \tag{10}$$

2.1.3. Tilt. The plate at height h above the magnet is now tilted around the y-axis in clockwise direction by a tilt angle α, figure 5. The tilt angles are assumed to be small ($\alpha \leqslant 1°$), therefore at an angle θ, α is reduced to γ according to equation (11). A cross-section of the bearing at angle θ is

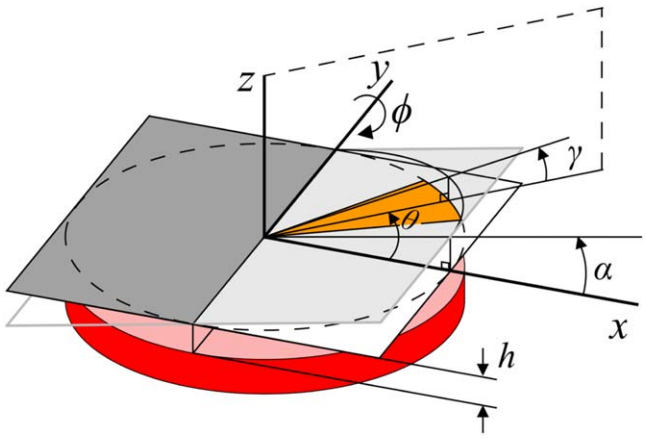

Figure 5. Schematic representation of the tilted bearing. The plate is tilted around the y-axis by an angle α. A cross-section of the bearing at the angle θ is shown in figure 6.

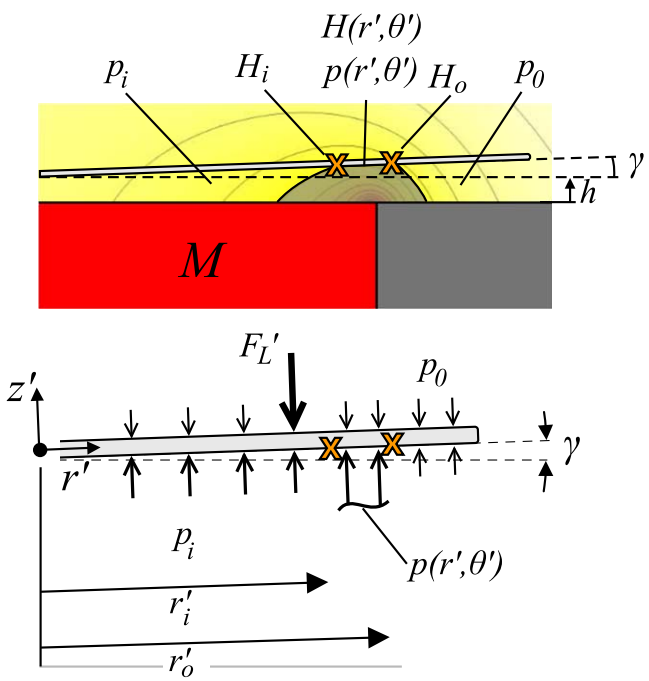

Figure 6. The shape of the ferrofluid seal and the resulting pressure distribution over the seal for a tilted bearing. Note that a body fixed frame of reference is introduced in the center of mass of the plate and that the tilt angle γ is introduced.

given in figure 6. This figure presents the pressure distribution that acts on the plate. Moreover, a body fixed frame of reference (r', θ', z') is introduced which will be used to calculate the load capacity and torque.

In contrast to equation (8), the pressure is now dependent on the angular coordinate θ', since the system is not axisymmetric any more. The total load capacity of the bearing perpendicular to the surface of the plate is obtained by combining equations (2) and (12), (13). The load capacity in vertical direction is approximately the same as the load capacity perpendicular to the surface of the plate for small tilt angles ($F_L \approx F_L'$). Note that in this analysis, part of the resultant force F_L', acting in r-direction due to the tilt, is neglected. This force accelerates the plate and possibly results in the plate gliding off the ferrofluid

$$\gamma = \alpha \cos(\theta), \tag{11}$$

$$F_L' = \int_0^{2\pi} \int_0^{r'_o(\theta')} (p(r', \theta') - p_0) r' \, \mathrm{d}r' \, \mathrm{d}\theta', \tag{12}$$

$$F_L' = \mu_0 M_s (H_i - H_o) \int_0^{2\pi} \int_0^{r'_i(\theta')} r' \, \mathrm{d}r' \, \mathrm{d}\theta' + \mu_0 M_s \int_0^{2\pi} \int_{r'_i(\theta')}^{r'_o(\theta')} (H(r', \theta') - H_o) r' \, \mathrm{d}r' \, \mathrm{d}\theta'. \tag{13}$$

Next, the torque that acts on the plate around the y-axis (M_y) can be calculated by multiplying the pressure distribution with its lever arm and integrating it over the entire area of the bearing, equation (14). Note that this is easily done in the body fixed frame of reference since the pressure distribution acts normal to the plate. Due to symmetry the resulting torque around the x-axis is zero

$$M_y = \int_0^{2\pi} \int_0^{r'_o(\theta')} -(p(r', \theta') - p_0) r' \cos(\theta') r' \, \mathrm{d}r' \, \mathrm{d}\theta'. \tag{14}$$

Finally, the tilt stiffness of the bearing (k_ϕ) around the y-axis (ϕ-direction) can be calculated by taking the derivative of the torque with respect to the tilt angle, equation (15). The negative sign is missing since the angle α is defined in the negative ϕ-direction

$$k_\phi = \frac{\mathrm{d}M_y}{\mathrm{d}\alpha}. \tag{15}$$

The sensitivity of the load capacity and operational range with respect to tilt will be included in the sensitivity analyses. Moreover, the effects of the saturation magnetisation and the applied volume of ferrofluid are included, see the results in section 3.

2.1.4. Mass inside pocket. If the pressure inside the pocket exceeds the maximum pressure the seal can withstand with respect to ambient pressure (equations (4) and (16*a*)), the seal breaks, air escapes and the bearing loses mass until equilibrium can be obtained again (figure 3 and equation (5)), as observed by Lampaert *et al* [34]. Consequently, this mass loss changes the characteristics of the bearing, namely the load capacity and stiffness. Mass gain also changes the characteristics. When the pressure difference over the seal exceeds the minimum strength of the seal (equations (6) and (16*c*)) it breaks. The result is that air surrounding the bearing moves through the seal into the air pocket. This process continues until the bearing gained sufficient air mass such that equilibrium can be obtained again, (figure 4 and equation (7)).

By introducing the ideal gas law in the calculations, the equilibrium position of the seal becomes dependent on the air mass enclosed by the ferrofluid seal, equations (3) and (16*b*). Compression and decompression of the bearing are assumed to be done in a slow fashion, such that the system can

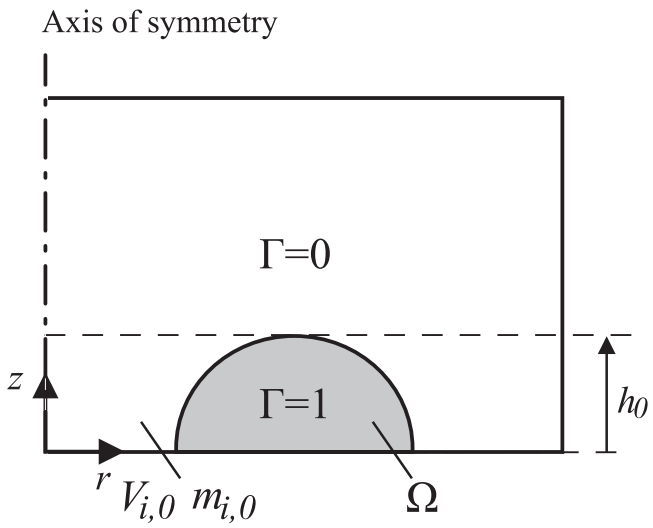

Figure 7. Air and ferrofluid are distinguished by the function Γ in the FEM.

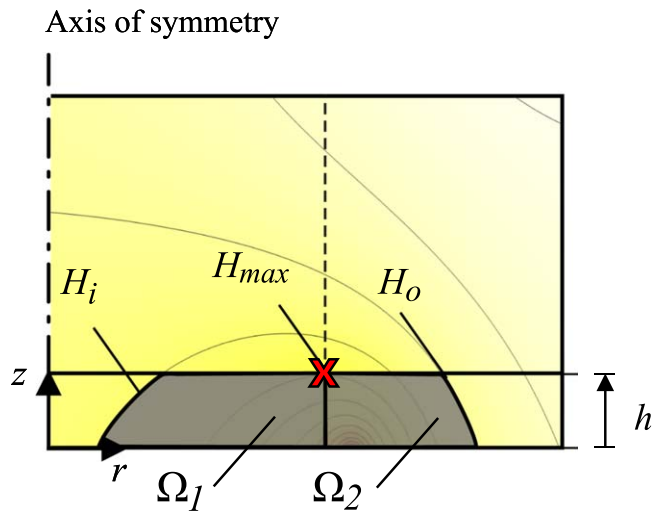

Figure 8. The ferrofluid domain ($\Gamma = 1$) is divided into the sets Ω_1 and Ω_2, which are defined by H_i, H_o, H_{max} and h.

continuously adjust itself to the temperature of the surroundings. Therefore, it is reasonable to assume an isothermal process, $\overline{R}T=$ Constant, with the temperature assumed to be room temperature, $T = 293$ K. The molar mass of air is denoted by M_{air} and the universal gas constant by $\overline{R}$. Initially, the mass of air inside the pocket is $m_{i,0}$, which is defined as the mass encapsulated by the seal at the fly height h_0, figure 7

$$p_i > p_{i,max} \text{ Loosing mass,} \tag{16a}$$

$$p_{i,min} \leqslant p_i \leqslant p_{i,max} \text{ Constant mass,} \tag{16b}$$

$$p_i < p_{i,min} \text{ Gaining mass.} \tag{16c}$$

2.2. FEM implementation

The goal of the FEM is to calculate the magnetic field produced by the magnet and subsequently to calculate the equilibrium position of the ferrofluid seal for varying m_i, V_{ff}, α, M_s and h. Using the position of the seal, the load capacity and torque can be calculated and the total behaviour of the bearing is obtained.

The shape and position of the ferrofluid seal for an arbitrary fly height h, is completely defined by the two variables H_i and H_o, figure 8. Therefore, an additional formulation (Γ), dependent on these variables, is introduced in the FEM, in order to distinguish air and ferrofluid, figure 7 and equation (17). $\Gamma = 1$ for all the coordinates which are part of the union of the sets Ω_1 and Ω_2 and indicates ferrofluid. Air is defined by $\Gamma = 0$, therefore volume integration of Γ results in the total amount of ferrofluid present in the system, equation (18). Next, the solving strategies for a perfectly aligned bearing as well as a tilted bearing will be discussed

$$\Gamma(r, z, \theta) = \begin{cases} 1 \text{ if } (r, z, \theta) \in (\Omega_1 \bigcup \Omega_2) & \text{Ferrofluid} \\ 0 \text{ if } (r, z, \theta) \notin (\Omega_1 \bigcup \Omega_2) & \text{Air} \end{cases}, \tag{17}$$

$$V_{ff} = \iiint \Gamma(r, z, \theta) \mathrm{d}V. \tag{18}$$

2.2.1. Perfect alignment. When there is no tilt, the system is axisymmetric which simplifies Γ to $\Gamma(r, z)$. Therefore, the system is modelled in COMSOL Multiphysics® (COMSOL Inc. version 5.3.1.348) as 2D axisymmetric. First, the magnetic field generated by the magnet is calculated. Subsequently, the equilibrium position of the ferrofluid seal is calculated by combining all the different forces (equations (2) and (3)) with the description for the ferrofluid (equations (17) and (18)). The calculations start from the fly height h_0 with the initial mass $m_{i,0}$ inside the pocket with volume $V_{i,0}$, figure 7. The characteristic of the aligned bearing is obtained by calculating the position of the ferrofluid for different fly heights. An overview of the solving strategy is given in figure 9.

2.2.2. Tilt. Due to the tilt, the system is not axisymmetric any more, figure 5. Therefore, the previously described solving strategy cannot be used any more. The problem can still be solved by modelling it in 3D, however this becomes computational expensive when more accuracy is needed. In order to reduce computational cost, the tilted bearing will be approximated by implementing a 2D (middle) Riemann sum, in which the pressure distribution at the centerline of each individual part k, represents the pressure distribution of that entire part. The interval and size β of each partition is determined by the number of subdivisions N, figure 11 and equation (19).

To illustrate this, the pressure distribution of partition k simplifies from $p(r', \theta')$ to $p(r', \theta = \beta k)$ on the interval between its lower boundary ($\theta_{l,\,k}$) and upper boundary ($\theta_{u,\,k}$). Note that the tilt angles are small ($\alpha \ll 1°$), therefore the angular coordinate θ is approximately the same in the global and body fixed frame of reference ($\theta' \approx \theta$). The cross-section presented in figure 6 corresponds to the centerline of the

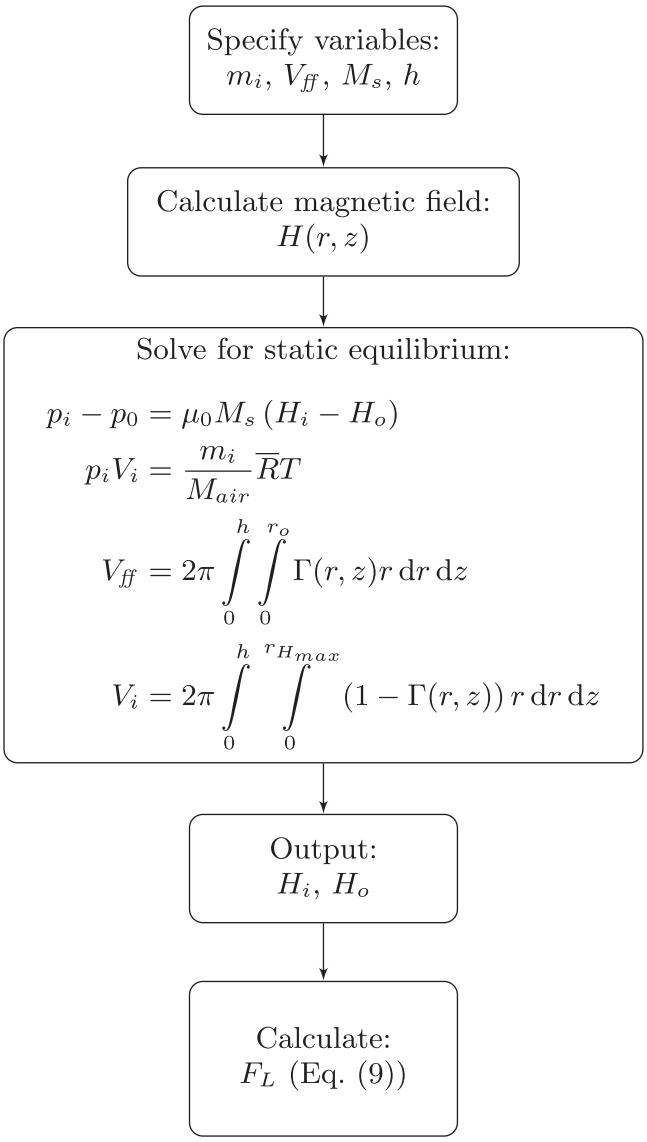

Figure 9. The solving strategy for the aligned (axisymmetric) ferrofluid bearing.

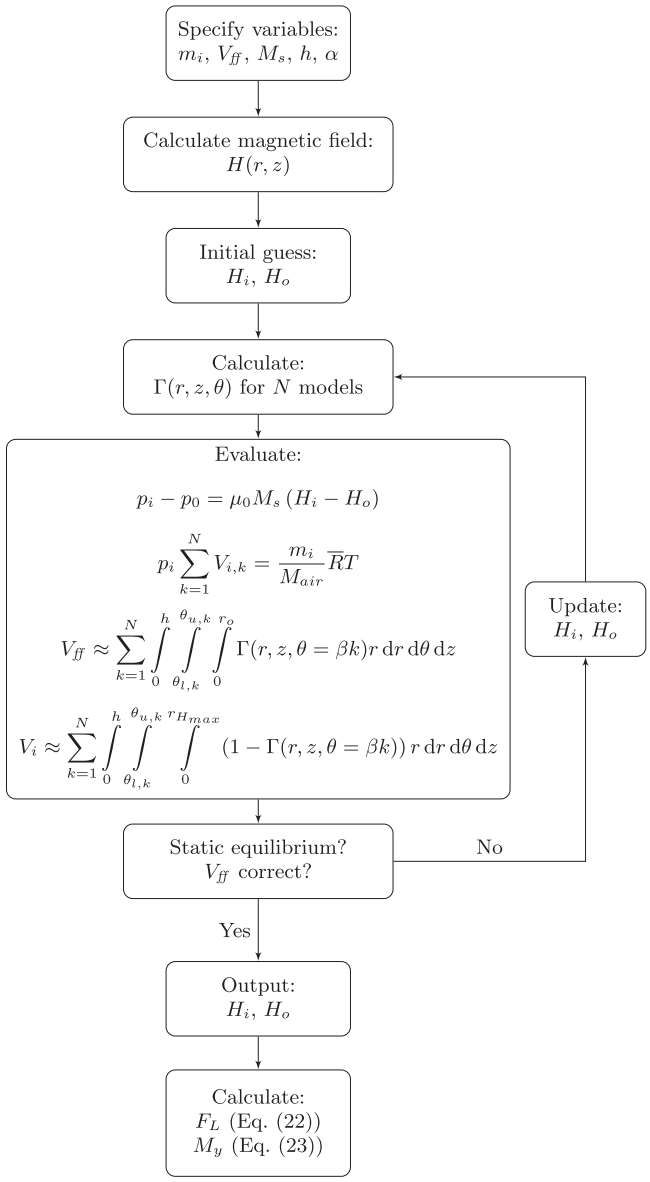

Figure 10. The solving strategy for the tilted (asymmetric) ferrofluid bearing.

orange partition presented in figures 5 and 11. Note that increasing the number of elements increases the accuracy of the approximation but also increases computational time. The convergence study showed that a physics-controlled mesh size 5 and $N = 16$ are required to obtain a relative error below 0.5%, see result in figure 15. The torque of the bearing (M_y) showed to be the most sensitive to small variations in the calculated equilibrium position of the ferrofluid. Therefore, M_y is used to quantify the convergence of the calculation. Note that M_y is scaled with respect to the finest and therefore assumed the most accurate calculation. This calculation was performed using a physics-controlled mesh size 1 and $N = 56$.

The advantage of the discretization is that each partition can be modelled using a 2D axisymmetric model, each with a slightly different tilt angle ($\gamma_k \approx \alpha\cos(\theta = \beta k)$, equation (11)). The disadvantage is that N calculations are needed. The model is solved for static equilibrium in an iterative fashion for the variables H_i and H_o, figure 10. The fminbnd algorithm in the MATLAB® R2018a Optimisation Toolbox™ (The MathWorks Inc.) is used in combination with the Livelink for the finite element calculations in COMSOL Multiphysics®. When H_i and H_o are known, both the load capacity and torque of the tilted bearing (equations (13) and (14)) can be calculated using the discretization, equations (20) and (21). Note that the lever arm of the pressure distribution can be approximated as $r'\cos(\theta)$ for small tilt angles

$$\beta = \frac{2\pi}{N}, \tag{19}$$

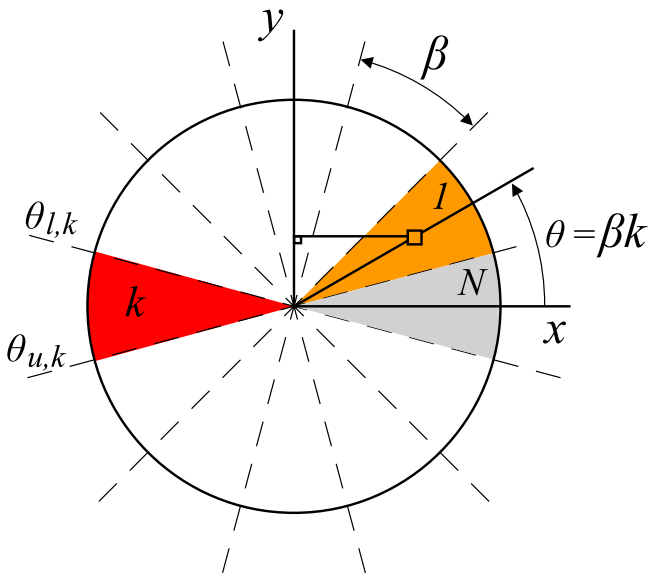

Figure 11. The discretization of the tilted bearing (figure 5) in a top view. The lever arm around the y-axis of a small pressure element is displayed.

$$F_L \approx \sum_{k=1}^{N} \int_{\theta_{l,k}}^{\theta_{u,k}} \int_0^{r'_o(\theta=\beta k)} (p(r', \theta = \beta k) - p_0) r' \mathrm{d}r' \mathrm{d}\theta, \tag{20}$$

$$M_y \approx \sum_{k=1}^{N} \int_{\theta_{l,k}}^{\theta_{u,k}} \int_0^{r'_o(\theta=\beta k)} - (p(r', \theta = \beta k) - p_0) r' \cos(\theta) r' \mathrm{d}r' \mathrm{d}\theta. \tag{21}$$

2.3. Experimental set-up

The presented model was validated by comparing the results of the theoretical model and the experiments that were performed as described below. In the validation, both the load capacity and stiffness were compared and discussed.

Experiments were performed using a test set-up as shown figures 12 and 13. A Zwick/Roell Z005 was used to measure the force over displacement behaviour of the bearing. The relative accuracy of the force measurement is 0.21%, whereas the repeatability has an accuracy below 0.33%. For the displacement measurement, the repeatability is 0.3 μm and the accuracy is 0.6 μm.

The ferrofluid bearing under testing consisted of a cylinder magnet, HKCM 9961-835, with a radius of 40 mm, a height of 10 mm and a remanent flux density of 1.28 T, placed in an aluminium casing. Next, the magnet attached to the aluminium casing, chosen for its non-ferromagnetic properties, was placed onto a low-grade steel plate. This is convenient since no glue or other connections were needed for the connection of the base plate and magnet. Finally, the magnet was mounted onto the testing machine using stainless steel bolts and aluminium clamps, figure 12. It is important to note that the head of the tensile testing machine was made of aluminium. If the material would be ferromagnetic, the force measurement would be errored, since the magnet would attract the head of the machine.

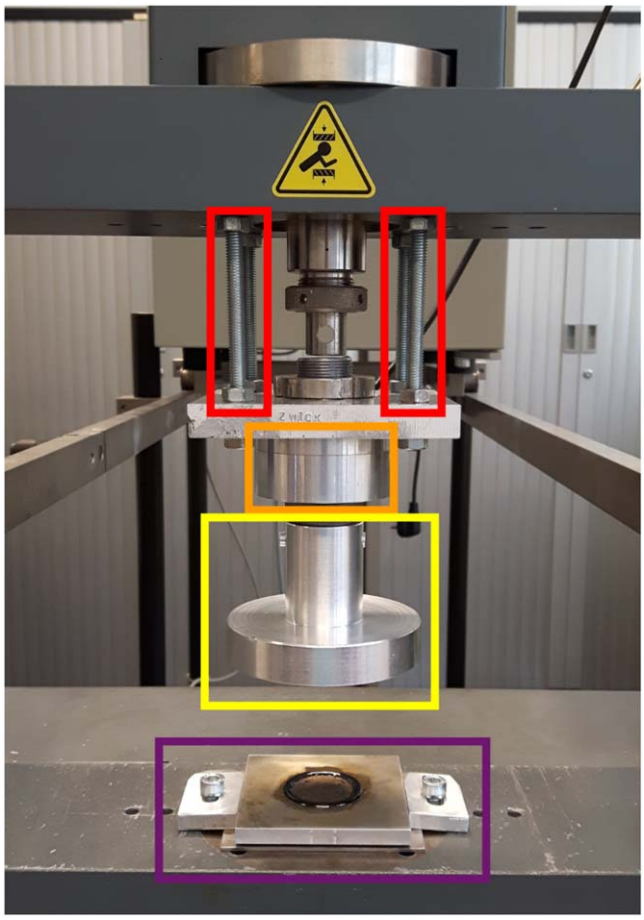

Figure 12. The test set-up consists of the ferrofluid bearing (purple), the head of the tensile testing machine (yellow) and the load cell (orange). The stiffness of the test set-up is approximately 2×10^6 N m^{-1}.

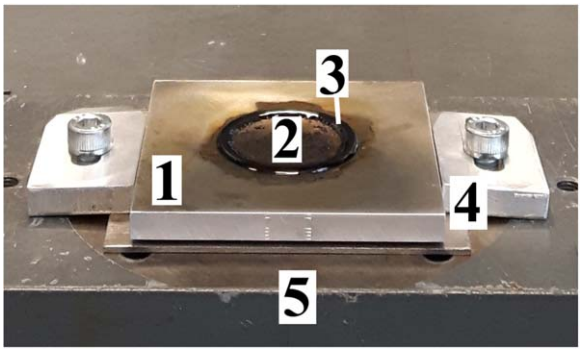

Figure 13. The ferrofluid bearing consists of the cylinder magnet (2) which is placed inside the aluminium casing (1) and the ferrofluid (3). The bearing is mounted to tensile testing machine (5) using clamps, bolts and a steel base plate (4).

2.3.1. Initialisation. Before the measurement started, the test set-up had to be prepared properly, meaning alignment of the machine and bearing, application of the ferrofluid and determination of the position of the surface of the bearing. This was done in the following manner: the head of the tensile tester was pressed onto the bearing with a force of 100 N, in

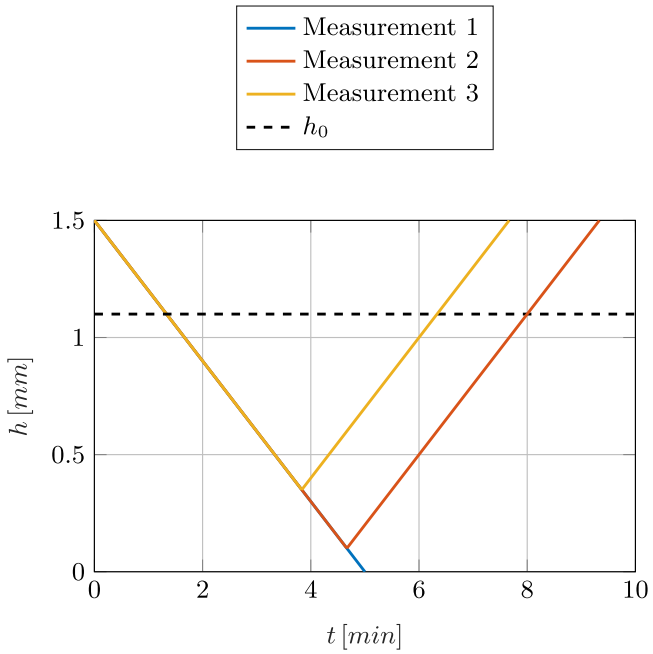

Figure 14. The position of the tensile testing machine (fly height h) versus the time for the different measurements. All three measurements start 1.5 mm above the surface of the magnet. h_0 indicates the height of the ferrofluid seal.

order to determine the position of the surface of the bearing, $h = 0$ mm, and the stiffness of the test set-up, approximately 2×10^6 N m^{-1}. At $h = 0$ mm, the surface of the head was aligned to the surface of the bearing using the nuts and bolts, red marking in figure 12.

Next, the head was retracted and ferrofluid was applied to the system using a pipette. The pipette is slightly inaccurate, since the ferrofluid was pulled out of the nozzle due to the magnetic attraction of the magnet onto the ferrofluid. Therefore, the mass of the pipette filled with ferrofluid was measured before and after application of the ferrofluid, using a weigh scale with an uncertainty of 0.005 g. By combining the density of the ferrofluid, $\rho = 1380$ kg m^{-3}, and the difference in mass, which corresponds to the applied mass of ferrofluid, the applied volume could be calculated.

The ferrofluid used in the measurements is the Ferrotec APG 513A, which has a saturation magnetisation of $M_s = 32$ kA m^{-1} at a temperature of 300 K. The applied volume of ferrofluid in the measurements was 0.38 ml.

2.3.2. Measurements. Before the actual measurements, an initial pre-wetting step was performed. This means compressing the bearing maximally until the head reaches $h = 0$ mm. This was done in order to apply a thin film of ferrofluid onto the head of the tensile testing machine, such that the experiments performed afterwards were repeatable. The thin film of ferrofluid only has to be applied once. Effectively, this means that the applied volume of 0.38 ml is slightly decreased.

After the pre-wetting step, three different measurements were performed, figure 14. First, the maximum load capacity of the bearing was measured by completely compressing the bearing until $h = 0$ mm. During the second and third measurement, the bearing was compressed until heights of 0.1 mm and 0.35 mm respectively, after which the bearing was fully decompressed. All the measurements were performed with a speed of 0.3 mm min^{-1}.

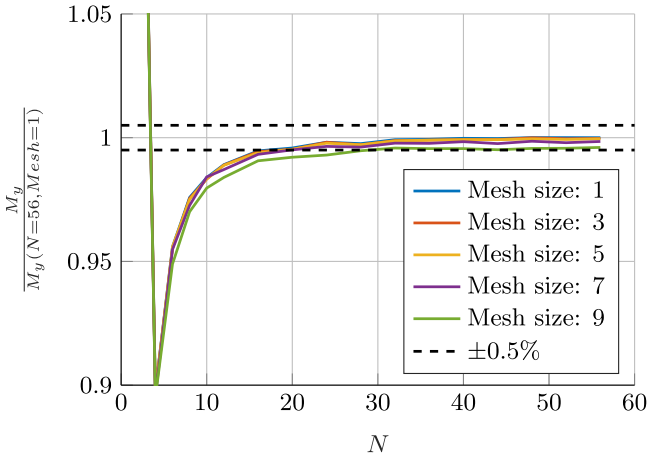

Figure 15. The accuracy of the discretized model (figure 11) with respect to the number of discretizations N. The convergence of the mesh size and discretization is determined by scaling the torque M_y with respect to the finest and therefore assumed the most accurate result, obtained using mesh size 1 and $N = 56$.

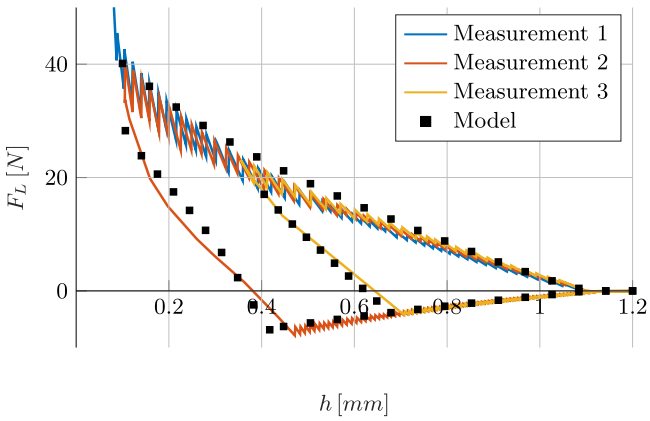

Figure 16. The modelled load capacity is compared to the measurement results. The maximum load capacity is given in blue, while red and yellow indicate two different compression and decompression cycles.

3. Results

The results of the convergence study are given in figure 15. Initially, when the number of discretizations N is small the relative error is >5%. Increasing the number of discretizations increases the accuracy of the model. In contrast, the convergence is fairly independent of the chosen physics-controlled mesh size. A physics-controlled mesh size 5 and $N = 16$ result in an error below 0.5%.

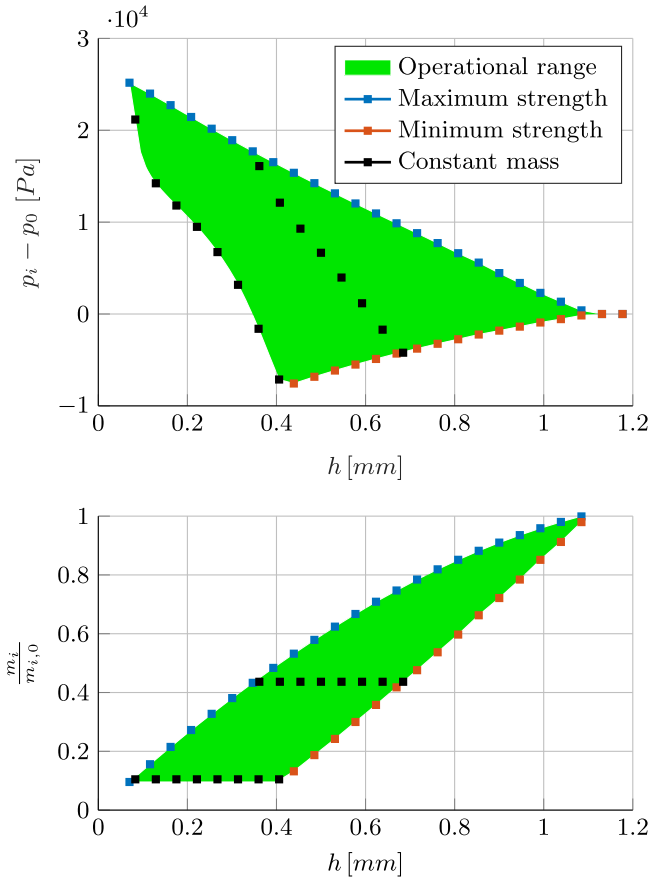

Figure 17. The pressure difference the ferrofluid seal can withstand calculated using the presented model (top figure) ket bearing (bottom figure). Decreasing the fly height increases the maximum and minimum strength of the ferrofluid seal, but decreases the air mass inside the pocket. The black markers correspond to measurements 2 and 3 from figure 16.

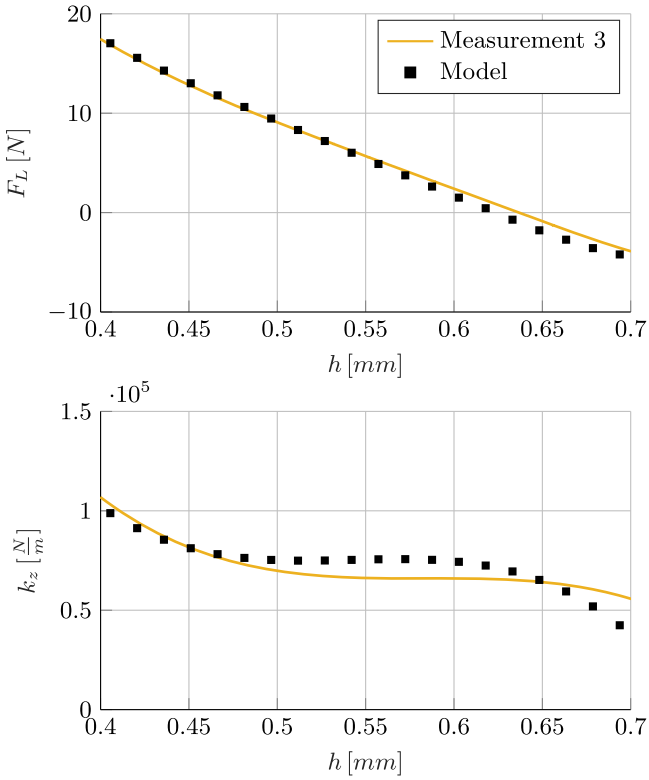

Figure 18. The load capacity (top figure) and stiffness (bottom figure) of the bearing, in the operational range of measurement 3 (figure 16), are compared to the model.

Next, the results of the measurements described in section 2.3.2 are given in figure 16. In this figure, the load capacity of the ferrofluid pocket bearing is shown versus the fly height for both the measurements and the model. The expected load capacity, calculated using the suggested model, is shown with black markers, while the different measurements are indicated with continuous lines.

Figure 17 shows the pressure and mass inside the pocket of the ferrofluid bearing versus the fly height. Note that the values correspond to the values of the model given in figure 16. These results are used to explain and interpret the behaviour of the bearing, namely the mass loss and operational range. In the top figure, the blue colour indicates the maximum pressure that the ferrofluid seal can withstand at that fly height, see also figure 3. The corresponding mass inside the pocket at maximum pressure is given in the bottom figure in blue. Note that the mass is normalised with respect to the initial mass $m_{i,0}$, figure 7. The red colour indicates the minimum pressure that the seal can withstand, see also figure 4. The corresponding mass inside the pocket is given in the bottom figure in red. The black lines correspond to measurements 2 and 3 of figure 16. The operational range of the ferrofluid pocket bearing is coloured green.

In the top figure of figure 18, the part of measurement 3 (figure 16) that is located in the operational range of the bearing according to figure 17, is presented. The bottom figure of figure 18 shows both the stiffness of the bearing derived from the load capacity measurements, as well as the stiffness derived from the load capacity predicted by the model.

Lastly, the sensitivity of the load capacity and operational range with respect to the saturation magnetisation of the ferrofluid (figure 19), the applied volume of ferrofluid (figure 20) and the tilt (figure 21) are given. The load capacity of the bearing significantly increased when the saturation magnetisation increased. The operational range did not change significantly when the saturation magnetisation was increased from 20 to 40 kA m^{-1}. Figure 20 shows that increasing the amount of ferrofluid increases both the load capacity and operational range. In contrast, figure 21 shows that tilt decreases both.

Figures 22 and 23 present the torque and the tilt stiffness with respect to the tilt angle for both the maximally and minimally pressurised pockets. Both figures globally show the same behaviour. When the tilt angle is positive, the torque and tilt stiffness are positive for all the different fly heights. The torque and tilt stiffness increase when the fly height is decreased or when the tilt angle is increased. When the pocket of the bearing was minimally pressurised, the magnitude of

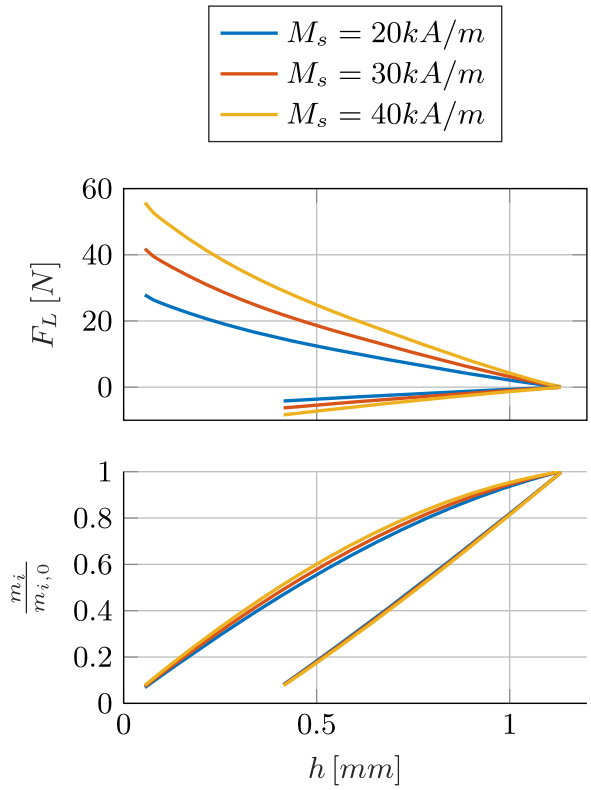

Figure 19. The modelled sensitivity of the load capacity (top figure) and the operational range (bottom figure), with respect to the saturation magnetisation. The other parameters correspond to the measurements, $V_{ff} = 0.38$ ml and $\alpha = 0°$. The air mass inside the pocket is normalised with respect to the initial mass of $M_s = 40$ kA m^{-1}.

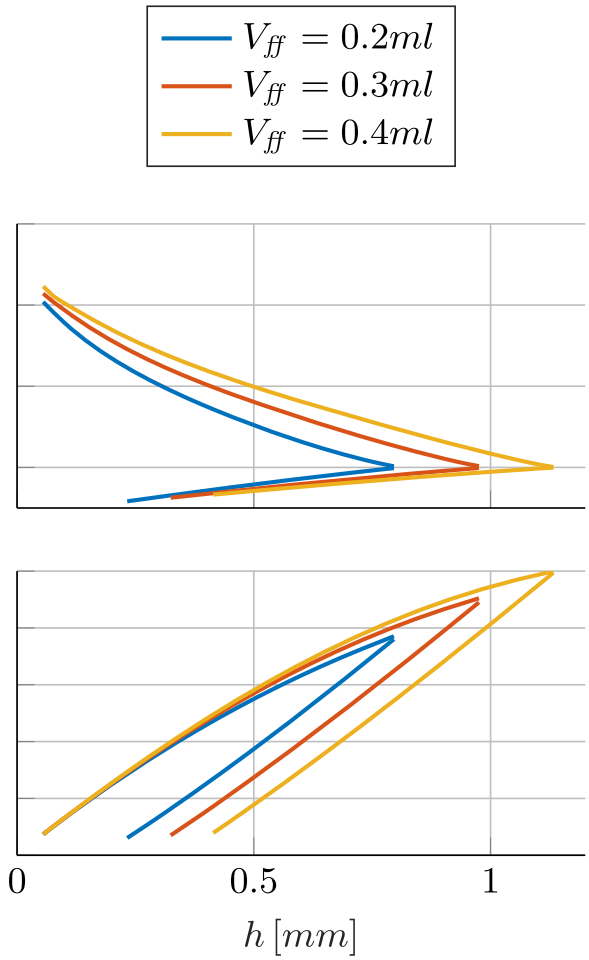

Figure 20. The modelled sensitivity of the load capacity (top figure) and the operational range (bottom figure), with respect to the applied volume of ferrofluid. The other parameters correspond to the measurements, namely $M_s = 0.32$ kA m^{-1} and $\alpha = 0°$. The air mass inside the pocket is normalised with respect to the initial mass of $V_{ff} = 0.4$ ml.

both the torque and tilt stiffness are lower when compared to the maximally pressurised pocket.

4. Discussion

4.1. Model validation: load capacity and operational range

All three measurements given in figure 16 show a zig–zag pattern, indicating that the mass of air inside the pocket changes. Either mass is gained or mass is lost. When the bearing is compressed, the pressure inside the pocket increases and the load capacity increases. When the pressure increases such that the strength of the ferrofluid seal is exceeded, mass escapes out of the pocket, as described in section 2.1.4. During decompression, the pressure inside the pocket decreases. When the ferrofluid seal cannot withstand the pressure difference any more, mass is gained. Thus, the strength of the ferrofluid seal defines the maximum and minimum load capacity of the bearing, which increase when the fly height is decreased. Overall, both the load capacity and stiffness of the ferrofluid pocket bearing seem to be accurately described by the suggested model, figures 16 and 18.

Measurements 2 and 3 showed that the behaviour of the bearing during decompression differs from the behaviour found during the initial compression. This phenomenon can be explained by the fact that mass is lost during the initial compression, which changes the system and therefore its characteristics. The zig–zag pattern is not present in the measurements during decompression of the bearing, indicating constant mass. After the minimum strength of the seal gets exceeded, or minimum load capacity, mass is gained and the system changes again. The behaviour of the bearing is repeatable and predictable in the operational range.

The operational range of measurement 3 is well described by the model. In contrast, measurement 2 shows that decompression of the bearing, after almost maximum compression, is less accurately described by the model. Inaccuracy of the model at these low fly heights could possibly be explained by the neglected surface effects, like capillary effects and surface tension. Also, the FEM model neglects magnetisation of the ferrofluid in the calculations. Moreover, the FEM model is sensitive to sharp edges in the geometry and the relative mesh size at those edges, particularly at low fly heights. The measurement itself can also be errored at low

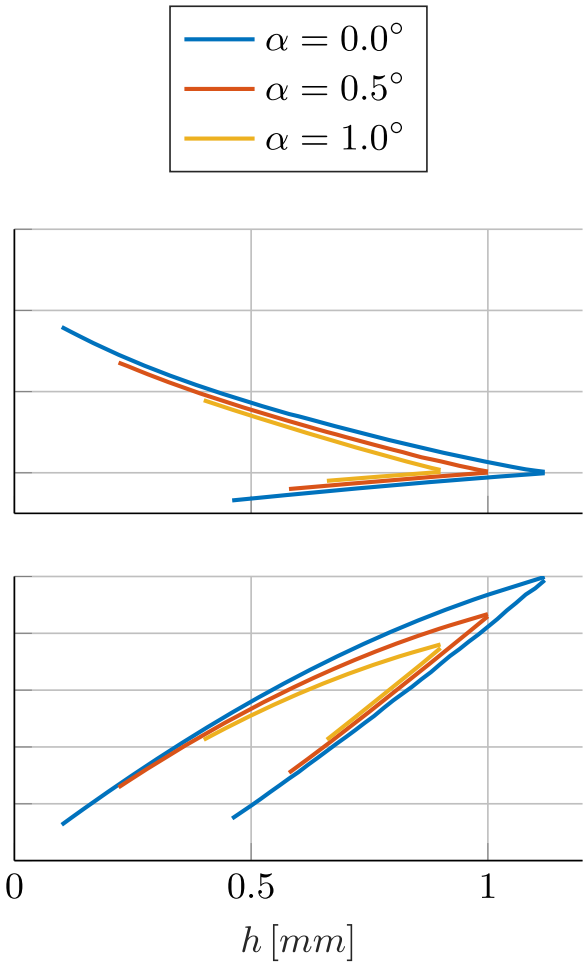

Figure 21. The modelled sensitivity of the load capacity (top figure) and the operational range (bottom figure), with respect to the tilting of the bearing. The other parameters correspond to the measurements, namely $V_{ff} = 0.38$ ml and $M_s = 0.32$ kA m^{-1}. The air mass inside the pocket is normalised with respect to the initial mass of $\alpha = 0.0°$.

fly heights due to for example a damaged magnet. Dents in the magnet result in magnetic field concentrations near the magnet. This effect becomes less pronounced further away from the magnet.

The stiffness of the test set-up is approximately 10 times the stiffness of the bearing. A force of 40 N, which is the approximately the load capacity of the bearing at a fly height of 0.1 mm, results in a displacement error of maximally 20 μm. Other uncertainties in the model are the saturation magnetisation of the steel base plate and the temperature of the environment. The temperature was not measured during the experiments, but is assumed to be approximately 293 K. The FEM model is able to calculate both static and dynamics problems. However, it is important to note that the model is limited to dynamic problems with relative low accelerations such that the problem can be approximated as quasi-static. This is because the FEM finds the positions of the interfaces between ferrofluid and air by solving for static equilibrium. In contrast, the FEM description makes it possible to include other forces, like capillary forces and surface tension, and to include magnetisation of the ferrofluid.

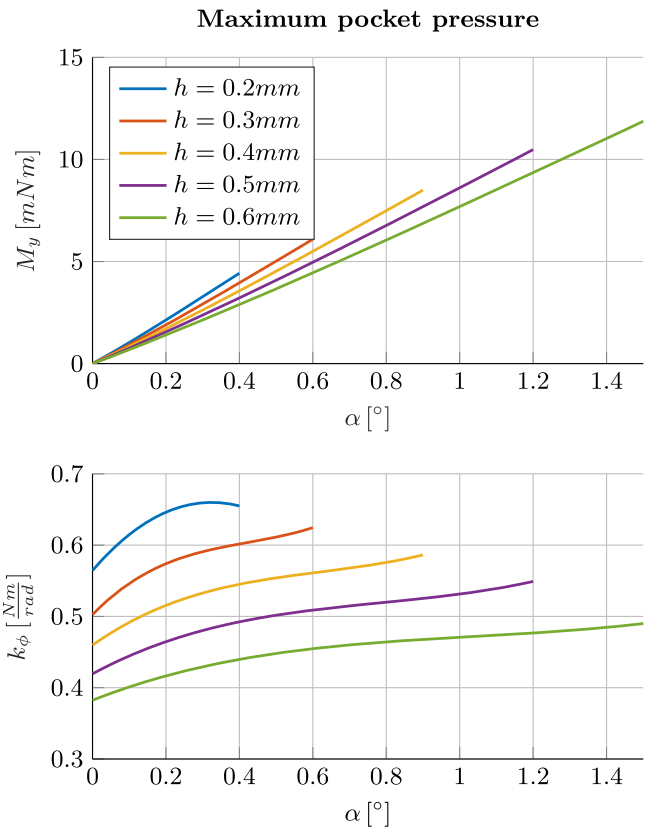

Figure 22. The tilt stiffness (bottom figure) of a maximally pressurised ferrofluid pocket bearing is a result of the torque around the y-axis (top figure), equation (15).

Figure 17 will be used to illustrate and explain the behaviour of figure 16 and to determine the operational range of the bearing. The operational range is indicated in green and is determined by the minimum and maximum pressure difference that the ferrofluid seal can withstand. When the fly height is decreased, the ferrofluid is pushed radially outwards causing ΔH to increase subsequently increasing the strength of the seal. Moreover, the magnetic field is stronger near the magnet thus compression of the bearing will also result in an increased ΔH. The combination of these two effects explains the increase in strength of the ferrofluid seal given in the top figure of figure 17.

The operational range of the bearing can easily be determined from figure 17, by looking at different constant mass lines or horizontal lines in the bottom figure. The intersection between a constant mass line and the green area indicates the operational range for that specific mass. Two examples are given with two sets of black markers. If the fly height is decreased beyond the operational range, mass is lost according to the set of blue markers. Afterwards, the new constant mass line can be used to determine the new operational range of the bearing. If the fly height is increased beyond the operational range, mass is gained according to the set of red markers. Thus, the operational range and behaviour of the bearing is determined by the initial compression, during which mass is squeezed out of the pocket. Note that ferrofluid bearings can easily be reset by separating the bearing and the plate.

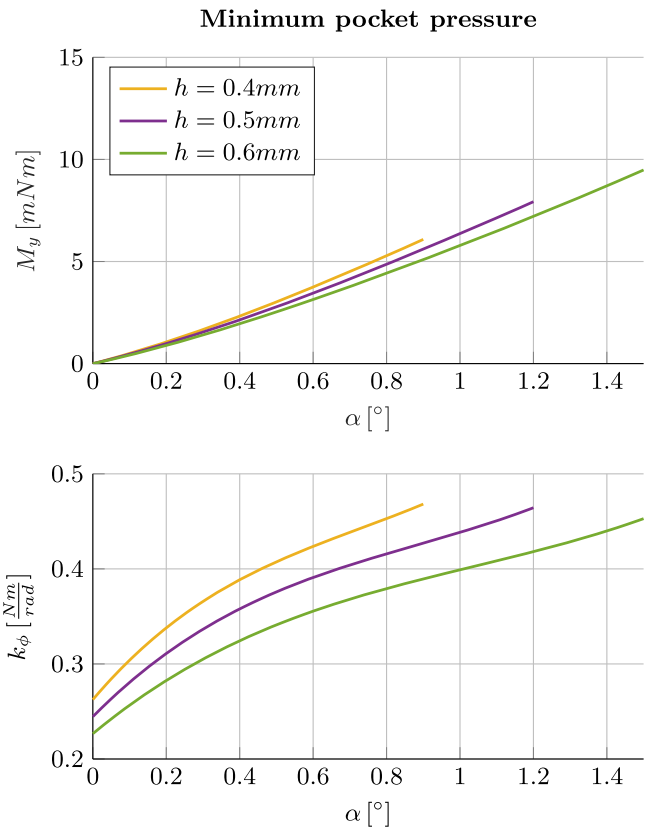

Figure 23. The tilt stiffness (bottom figure) of a minimally pressurised ferrofluid pocket bearing is a result of the torque around the *y*-axis (top figure), equation (15).

It can be concluded that the model properly describes the behaviour of the bearing, except at very low fly heights. It might be interesting for further research to model and measure the behaviour of multiple seals and pockets, or to use an incompressible fluid instead of air inside the pocket. In both cases, it might be convenient to measure the actual pressure inside the pocket instead of only measuring the force and displacement.

4.2. Sensitivity analysis

Only the three variables that are assumed to be the most erroneous during the actual measurements are discussed in the sensitivity analysis. Other variables, for example surface effects, are neglected in the sensitivity analysis, since they are either neglected or included in the derivation of the model on which the rest of the analysis is based on. The presented values in figures 19–21 are a bit exaggerated for errors that might occur in practice. However, this way the effect of the different errors becomes clearly visible. It is important to note that the effects the variables have on the load capacity and operational range of the bearing are evaluated individually. Combined effects are beyond the scope of this research, however they should be modelled and kept in mind when designing ferrofluid bearings for high precision systems.

Both tilt and the applied volume of ferrofluid have a significant influence on both the load capacity and the operational range. In contrast to increasing the tilt angle, increasing the amount of ferrofluid increases the operational range and load capacity. Addition of more ferrofluid increases the height of the ferrofluid ring, thus results in earlier contact and establishment of both the seal and air pocket. However, the effect of adding more ferrofluid decreases at low fly heights. When the bearing is almost entirely compressed, the outer interface H_o is nearing zero, so addition of more ferrofluid does not increase ΔH significantly any more. In contrast, both saturation magnetisation and tilt change the behaviour of the bearing at every fly height. The load capacity of the bearing significantly increases when the saturation magnetisation increases. This increase is linear according to equations (1) and (9). It is also worth noticing that the operational range of the bearing is limited by tilting of the plate. Higher tilt angles result in earlier contact of the plate with the bearing surface, thus limiting the operational range. Moreover, tilt decreases the height at which the enclosed air pocket is established, resulting in a decreased load capacity and operational range. Accordingly, some general design guidelines for ferrofluid bearings can be formulated. (1) Tilt of either the plate or the bearing should be minimised, since tilt decreases the load capacity and the operational range. (2) Increasing the volume of ferrofluid increases the load capacity and operational range. Ferrofluid should therefore be added to the system, until the point of diminishing returns.

The small difference between the measured and the predicted load capacity can possibly be explained by the errors discussed here. Since only three possible errors are discussed, no conclusions can be drawn regarding which set of errors was present in the measurements. However, slight overestimation of the amount of ferrofluid is likely, since a ferrofluid trail is left behind on the head of the testing machine after the initial compression.

Figures 22 and 23 show that the tilt stiffness of the bearing is positive for positive tilt angles, for both maximum and minimum pressure inside the pocket. Since the system is symmetric, the tilt stiffness is also positive for negative tilt angles. Therefore, due to the positive tilt stiffness, it can be concluded that the ferrofluid bearing is self-aligning regardless of the pressure inside the pocket. However, in order to be certain that the described behaviour of the ferrofluid bearing is indeed correct, it is recommended that for future work the load capacity and torque of the bearing are actually measured for different tilt angles.

5. Conclusion

This article provides a simple and efficient way to obtain the operational range of a ferrofluid pocket bearing from only the mass versus fly height diagram. The operational range is only dependent on the magnetic field produced by the magnet and the amount of ferrofluid present in the system.

The experimentally validated model accurately describes the load characteristic of a ferrofluid pocket bearing. The model includes the air mass inside the pocket, since both the load capacity and stiffness of the bearing change when the mass changes. Overcompression of the bearing results in mass loss and overdecompression in mass gain. The bearing

shows repeatable and predictable behaviour when the mass inside the pocket does not change. In practice, this is the operational range of the bearing.

The operational range of the bearing is sensitive to errors such as tilt or uncertainty in the applied volume of ferrofluid. The sensitivity analysis shows that tilt decreases both the load capacity and operational range of the bearing. Independent of the pressure inside the pocket, both the torque acting on the plate above the bearing and the resulting tilt stiffness are always positive when tilted. It can be concluded that ferrofluid pocket bearings are always self-aligning. The tilt stiffness increases when the fly height decreases or when the tilt angle increases. Increasing the amount of ferrofluid increases the operational range of the bearing significantly while the load capacity is only increased for higher fly heights.

ORCID iDs

S G E Lampaert https://orcid.org/0000-0002-8268-1457

References

[1] Rosensweig R E 2013 *Ferrohydrodynamics* (New York: Dover) p 368
[2] Shliomis M I 1974 *Sov. Phys.—Usp.* **17** 153
[3] Scherer C and Neto A F 2005 *Braz. J. Phys.* **35** 718
[4] Raj K, Moskowitz B and Casciari R 1995 *J. Magn. Magn. Mater.* **149** 174
[5] Raj K and Moskowitz R 1990 *J. Magn. Magn. Mater.* **85** 233
[6] Rinaldi C, Chaves A, Elborai S, He X and Zahn M 2005 *Curr. Opin. Colloid Interface Sci.* **10** 141
[7] Urreta H, Aguirre G, Kuzhir P and Lopez de Lacalle L N 2018 *Int. J. Precis. Eng. Manuf.* **19** 495
[8] Torres-Díaz I and Rinaldi C 2014 *Soft Matter* **10** 8584
[9] Yang R-J, Hou H-H, Wang Y-N and Fu L-M 2016 *Sensors Actuators* B **224** 1
[10] Cheng H C, Xu S, Liu Y, Levi S and Wu S T 2011 *Opt. Commun.* **284** 2118
[11] Jayhooni S M H, Assadsangabi B and Takahata K 2018 *Sensors and Actuators* A **269** 258
[12] Olaru R, Petrescu C and Hertanu R 2012 *J. Intell. Mater. Syst. Struct.* **23** 1623
[13] Sudo S, Takaki Y, Hashiguchi Y and Nishiyama H 2005 *JSME Int. J.* B **48** 464
[14] Uhlmann E and Bayat N 2006 *CIRP Ann.—Manuf. Technol.* **55** 415
[15] Tipei N 1982 *J. Lubr. Technol.* **104** 510
[16] Liu Q, Alazemi S F, Daqaq M F and Li G 2018 *J. Magn. Magn. Mater.* **449** 105
[17] Rosensweig R 1970 *US Patent* US3620584A
[18] Rosensweig R E, Raj K and Black T J 2003 *US Patent* US6543782B1
[19] Mitamura Y, Takahashi S, Amari S, Okamoto E, Murabayashi S and Nishimura I 2011 *J. Artif. Organs* **14** 23–30
[20] Ravaud R, Lemarquand G and Lemarquand V 2010 *Tribol. Int.* **43** 76–82
[21] Rosensweig R 1987 *Annu. Rev. Fluid Mech.* **19** 437
[22] Potma O G R 2017 Designs for rotary shaft fluid seals in an aqueous environment using ferrofluid *Msc Thesis* Technical University Delft
[23] Arcire A, Olaru R and Petrescu C 2012 *EPE 2012—Proc. 2012 Int. Conf. Exposition on Electrical and Power Engineering* p 776
[24] Boots A, Krijgsman L, de Ruiter B, Lampaert S and Spronck J 2019 *Tribol. Int.* **129** 46–54
[25] Olaru R, Petrescu C and Arcire A 2013 Maximizing the magnetic force generated by an actuator with non-magnetic body in a ferrofluid pre-magnetized by permanent magnets *Int. Rev. Electr. Eng.* **8** 904
[26] Alvarez-Aguirre A, Mok G, HosseinNia S H and Spronck J W 2016 *2016 Int. Conf. on Manipulation, Automation and Robotics at Small Scales, MARSS 2016* (https://doi.org/10.1109/MARSS.2016.7561698)
[27] Deng R, van Veen S, Café M, Spronck J W and Schmidt R H M 2014 Linear nano-positioning stage using ferrofluid bearings *14th Euspen Int. Conf. (Dubrovnik, June 2014)* p 4
[28] Lampaert S, Spronck J, van Ostayen R and Café M 2014 (2+4) DOF precision motion stage with ferrofluid bearings *American Society for Precision Engineering* 63
[29] Lampaert S, Spronck J, van Ostayen R and Habib H 2016 XY360 – Planar Positioning Stage with a PSD sensor and ferrofluid bearings *DSPE Conference on Precision Mechatronics* p 57
[30] Millet G and Hubert A 2006 *Actuators'06* June, 656–59
[31] Lampaert S G E, Fellinger B J, Spronck J W and van Ostayen R A J 2017 *Precis. Eng.* **54** 163–70
[32] Petit M, Kedous-Lebouc A, Avenas Y, Tawk M and Artega E 2011 *Prz. Elektrotech.* **9b** 115–19
[33] Yu J, He X, Li D and Li W 2018 *Phys. Fluids* **30** 092004
[34] Lampaert S G E, Spronck J W and van Ostayen R A J 2017 *Proc. Inst. Mech. Eng.* J **232** 14–25
[35] Neuringer J L and Rosensweig R E 1964 *Phys. Fluids* **7** 1927